RSC Advances

PAPER

View Article Online
View Journal | View Issue

Enhanced hydrogen storage properties of $LiAlH_4$ catalyzed by $CoFe_2O_4$ nanoparticles†

Cite this: *RSC Adv.*, 2014, **4**, 18989

Ziliang Li,[a] Fuqiang Zhai,[b] Qi Wan,[a] Zhaojiang Liu,[a] Jiawei Shan,[a] Ping Li,*[a] Alex A. Volinsky[c] and Xuanhui Qu[a]

The catalytic effects of $CoFe_2O_4$ nanoparticles on the hydrogen storage properties of $LiAlH_4$ prepared by ball milling were investigated. The onset desorption temperature of the $LiAlH_4$ + 2 mol% $CoFe_2O_4$ sample is 65 °C, which is 90 °C lower that of the as-received $LiAlH_4$, with approximately 7.2 wt% hydrogen released at 250 °C. The isothermal desorption results show that for the 2 mol% $CoFe_2O_4$ doped sample dehydrogenated at 120 °C, 6.8 wt% of hydrogen can be released within 160 min, which is 6.1 wt% higher than that of the as-received $LiAlH_4$ under the same conditions. Through the differential scanning calorimetry (DSC) and the Kissinger desorption kinetics analyses, the apparent activation energy, E_a, of the 2 mol% $CoFe_2O_4$ doped sample is calculated as 52.4 kJ mol^{-1} H_2 and 86.5 kJ mol^{-1} H_2 for the first two decomposition processes. This is 42.4 kJ mol^{-1} H_2 and 86.1 kJ mol^{-1} H_2 lower compared with the pristine $LiAlH_4$, respectively, indicating considerably improved dehydrogenation kinetics by doping the $CoFe_2O_4$ catalyst in the $LiAlH_4$ matrix. From the Fourier transform infrared spectroscopy (FTIR) and X-ray diffraction (XRD) analyses, a series of finely dispersed Fe and Co species with a range of valence states, produced from the reactions between $LiAlH_4$ and $CoFe_2O_4$, play a synergistic role in remarkably improving $LiAlH_4$ dehydrogenation properties. The rehydrogenation properties of the $LiAlH_4$ + 2 mol% $CoFe_2O_4$ sample have also been investigated at 140 °C under 6.5 MPa pressure held for 2.5 h.

Received 29th January 2014
Accepted 18th March 2014

DOI: 10.1039/c4ra00841c

www.rsc.org/advances

1. Introduction

As a renewable energy source, hydrogen can be produced from water and biomass without any greenhouse gas emissions. Thus, hydrogen attracts considerable attention from research aiming to solve the fossil fuel depletion problem accompanied by the global environmental issues.[1–3] The prerequisite for widespread hydrogen use as an energy carrier is the development of advanced hydrogen storage materials for safely storing it at high gravimetric and volumetric densities.[4–6]

Among numerous possible hydrogen storage materials, lithium aluminum hydride[7–10] ($LiAlH_4$) is a promising candidate due to its relatively large theoretical hydrogen storage capacity and high potential reversible hydrogenation capability. Theoretically, $LiAlH_4$ can desorb 10.5 wt% hydrogen upon heating to 420 °C, which make it an ideal hydrogen storage material to meet the U.S. Department of Energy 2015 targets for a viable hydrogen storage system[11] with gravimetric density ≥5.5 wt% and volumetric density ≥40 g L^{-1}. Upon heating, $LiAlH_4$ would gradually release hydrogen, according to the following three steps.[12] The first reaction step (R1) occurs in the 150–175 °C temperature range and releases 5.3 wt% hydrogen:

$$3LiAlH_4 \rightarrow Li_3AlH_6 + 2Al + 3H_2 \quad (1)$$

Then the second reaction step (R2) occurs between 180 °C and 220 °C, releasing 2.6 wt% hydrogen:

$$Li_3AlH_6 + 2Al \rightarrow 3LiH + 3Al + 3/2H_2 \quad (2)$$

The third reaction step (R3) starts to release 2.6 wt% hydrogen above 400 °C:

$$3LiH + 3Al \rightarrow 3LiAl + 3/2H_2 \quad (3)$$

Thus, the dehydrogenation properties of $LiAlH_4$ are generally analyzed for the first two decomposition reactions due to the high onset and decomposition temperatures, and the low desorbed hydrogen content of the reaction R3 from the practical applications perspective.[13–16]

[a]*Institute for Advanced Materials and Technology, University of Science and Technology Beijing, Beijing 100083, China. E-mail: ustbliping@126.com; Fax: +86-10-62334311; Tel: +86-10-82377286*

[b]*Departament Física Aplicada, EETAC, Universitat Politècnica de Catalunya BarcelonaTech, 08860 Castelldefels, Spain*

[c]*Department of Mechanical Engineering, University of South Florida, Tampa, FL 33620, USA*

† Electronic supplementary information (ESI) available: XRD pattern for the as-milled $LiAlH_4$ doped with $CoFe_2O_4$ by using hand-milling method is provided in order to explain the fact that temperature is driving force for the reaction between $LiAlH_4$ and $CoFe_2O_4$. See DOI: 10.1039/c4ra00841c

Since Bogdanovic *et al.*[17] conducted the seminal work in improving the hydrogen storage performance of $NaAlH_4$ by doping $TiCl_3$, extensive efforts have been devoted to ameliorate the re/dehydrogenation properties of $LiAlH_4$ by adding various catalysts to lower its onset dehydrogenation temperature and increase its dehydrogenation kinetics. To date, the documented catalysts for $LiAlH_4$ can be classified as: (1) pure metals;[1,18–26] (2) carbon-containing species;[21,27–31] (3) metal halides;[13,19,21,32–42] (4) alloys;[18,20] (5) metal oxides[14–16,43,44] and (6) other compounds.[45–49] To our knowledge, a partial reversibility can be realized through doping $LiAlH_4$ with various catalysts.[28,35,44,50] However, the rehydrogenation property was not ideal. From the practical applications perspective, solid-state materials ($LiAlH_4$, $NaAlH_4$, MgH_2, *etc.*) do have the potential to outperform physical methods of storage (cryostorage or high-pressure technologies) through comprehensively considering the safety, environment friendless and cost, which has been reported in many review papers.[51,52] However, it is crucial to find an advanced catalyst, which could not only significantly improve the dehydrogenation, but also rehydrogenation performance of $LiAlH_4$. Recently the authors have observed the superior effects of Fe_2O_3 and Co_2O_3 nanoparticles on promoting the dehydrogenation properties of $LiAlH_4$, however, nano-sized Fe_2O_3 and Co_2O_3 failed to produce any reversibility for $LiAlH_4$.[15] Herein, it is reasonable to speculate that Co ferrite shows a great potential as the catalyst to advance hydrogen storage performance of $LiAlH_4$.

In this work, the catalytic efficiency of $CoFe_2O_4$ nanoparticles on the dehydrogenation and reversible hydrogenation properties of $LiAlH_4$ was evaluated by utilizing a pressure-composition-temperature (PCT) apparatus and differential scanning calorimetry (DSC). The catalytic mechanism of $CoFe_2O_4$ nanoparticles was demonstrated by analyzing the results of the Fourier transform infrared spectroscopy (FTIR), X-ray diffraction (XRD) and scanning electronic microscopy (SEM). The comparison of the catalytic effects of $CoFe_2O_4$, Fe_2O_3 and Co_2O_3 catalysts for $LiAlH_4$ is also presented in this work.

2. Experimental

2.1. Sample preparation

$LiAlH_4$ (≥95% pure) was purchased from the Sigma Aldrich Co., and $CoFe_2O_4$ (≥99.99% pure, 20 nm) was prepared by using the sol–gel method. The details of the preparation procedure are given in the previous report.[53] All handling of the samples was conducted in a glove box (Mikrouna Co., China) under high-purity argon atmosphere (H_2O: <10 ppm; O_2: <10 ppm) in order to minimize oxidation and humidity. About 1.5 g of $LiAlH_4$ was mixed with various mole fractions of $CoFe_2O_4$ nanopowder, and then the mixture was loaded into a stainless steel grinding vial (5 cm in diameter, quenching). After that, ZrO_2 balls (Mohs hardness ≥ 7.5) were added with a ball-to-powder weight ratio of 20 : 1 in the glove box. Finally, the grinding vial with the mixed sample was ball milled for 30 min by using a high energy Spex mill (QM-3B) at a milling rate of 1200 rpm. In order to prevent excess heating and the surface fatigue wear of ball-milling materials, the grinding vial was cooled down for 5 min after milling every 10 min.

2.2. Characterization

The hydrogen storage performance of the as-received and doped $LiAlH_4$ samples was measured by using a Sieverts-type PCT apparatus (Beijing Nonferrous Metal Research Institute, China). The PCT equipment can be heated up to 600 °C with a maximum hydrogen pressure of 10 MPa. To measure the dehydrogenation properties, 0.3 g sample was loaded into a stainless steel vessel and then heated to 250 °C at 5 °C min^{-1} heating rate under 0.1 atm pressure. For the rehydrogenation measurements, the samples that completed the first dehydrogenation were directly reheated at 150 °C under 6.5 MPa for 3 h. The de/rehydrogenation amount for all samples was calculated from the pressure changes, and then the values were converted for pure $LiAlH_4$ with the elimination of various impurities, the detailed calculation formula is as follows,

$$\text{mat-wt\%} = \text{H}_2\text{ mass}/[\text{mass (storage material)} + \text{mass (catalyst)} + \text{H}_2\text{ mass}] \quad (4)$$

All the weight percentage values we talked about in the present paper on materials (pure or doped sample) basis.

In order to investigate the decomposing behavior and calculate the activation energy of both as-received and doped $LiAlH_4$ samples, DSC measurements were conducted by using NETZSCH STA 449C under a flow of 50 mL min^{-1} high-purity Ar. Typically, about 5 mg of sample was sealed into a 50 mL alumina crucible in the glove box, and then was heated at different heating rates (6 °C min^{-1}, 9 °C min^{-1}, and 12 °C min^{-1}) from 35 °C to 300 °C, respectively.

The morphology of the as-received and 2 mol% $CoFe_2O_4$-doped samples were observed by SEM (ZEISS EVO 18, Germany) equipped with the energy dispersive spectroscopy (EDS) detector. Prior to the SEM observations, the samples were prepared inside the glove box, and then transferred to the SEM chamber in order to prevent oxidation and moisture adsorption.

FTIR analysis of the as-received and doped $LiAlH_4$ samples after ball milling was carried out by using Bruker Vector 22 FTIR spectrometer. The FTIR spectra were recorded between 2000 cm^{-1} and 750 cm^{-1} with a spectral resolution of 4 cm^{-1}.

Phase structure characteristics of the as-milled and de/rehydrogenated samples were detected by XRD (MXP21VAHF X-ray diffractometer with CuKα radiation, 40 kV, 200 mA) at room temperature. The X-ray intensity was tested over the 2θ angle ranged from 10° to 90° with a scanning velocity of 0.02° per second.

3. Results and discussion

Fig. 1 displays the non-isothermal desorption curves of the as-received $LiAlH_4$, as-milled $LiAlH_4$, and $LiAlH_4$ doped with 1 mol %, 2 mol%, 3 mol%, and 5 mol% $CoFe_2O_4$ nanoparticles, heated from 25 °C to 250 °C at a heating rate of 5 °C min^{-1}. As seen in Fig. 1, the as-received $LiAlH_4$ sample started to release hydrogen at around 155 °C and about 5.0 wt% hydrogen desorbed during the first dehydrogenation step. With increasing temperature, the as-received $LiAlH_4$ sample entered into the

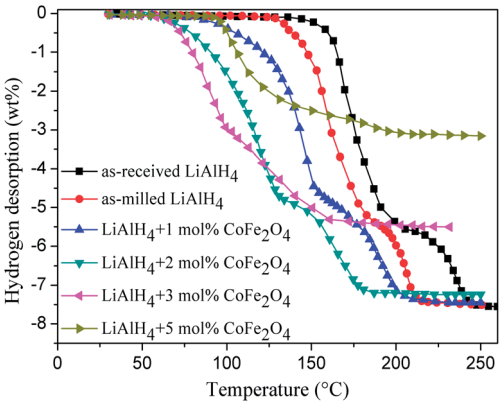

Fig. 1 Thermal desorption profiles of the as-received $LiAlH_4$, as-milled $LiAlH_4$, and $LiAlH_4$ doped with 1, 2, 3, and 5 mol% $CoFe_2O_4$ nanoparticles. The samples are heated to 250 °C at 5 °C min^{-1} heating rate.

second dehydrogenation step from 200 °C and about 2.5 wt% hydrogen was released at the second dehydrogenation stage. Thus, the total hydrogen release capacity of 7.5 wt% could be obtained when the as-received $LiAlH_4$ was heated to 250 °C. For the as-milled $LiAlH_4$ sample, the onset dehydrogenation temperature in the first two dehydrogenation steps deceased by about 21 °C, compared with the as-received $LiAlH_4$, mainly attributed to the surface activation, introduced to the $LiAlH_4$ matrix by mechanical milling.[13–16,24,28,38,39,42,43] Compared with the $LiAlH_4$ samples without any catalysts doping, the onset desorption temperature of $LiAlH_4$ doped with $CoFe_2O_4$ nanoparticles exhibited a remarkable reduction, not only for the first, but also for the second dehydrogenation step. When 1 mol% $CoFe_2O_4$ nanopowder was added to the $LiAlH_4$ matrix, the onset dehydrogenation temperature decreased by 75 °C for the first stage and 40 °C for the second stage, compared with the as-received $LiAlH_4$. The 1 mol% doped sample released 7.4 wt% hydrogen at the first two dehydrogenation steps. By further increasing the content of the $CoFe_2O_4$ nanoparticles to 2 mol%, the $LiAlH_4$ + 2 mol% $CoFe_2O_4$ sample started to release hydrogen at 65 °C and 130 °C for the first two dehydrogenation steps, which decreased by 90 °C and 70 °C, compared with the as-received $LiAlH_4$, respectively. Overall, 7.2 wt% hydrogen was released for the 2 mol% doped sample. For the hydrogen release content of 1 mol% and 2 mol% doped samples, they are close to the theoretical hydrogen release content of pristine $LiAlH_4$ (7.5 wt% H_2). For the 3 mol% $CoFe_2O_4$ doped sample, the onset dehydrogenation temperature further decreased to 61 °C for the first dehydrogenation step, while only 5.5 wt% hydrogen was released during the first two dehydrogenation processes, indicating a drastic reduction in the released hydrogen capacity after doping an excess amount of $CoFe_2O_4$ nanoparticles. A similar phenomenon was also proposed in previous reports.[13,14,28,35,37,43,47] However, when 5 mol% of $CoFe_2O_4$ were added, the $LiAlH_4$ doped sample started to dehydrogenate at 100 °C, which is much higher than the other contents $CoFe_2O_4$-doped samples. Meanwhile, the desorption hydrogen content dropped sharply to 3.2 wt% for the first two dehydrogenation steps, which only accounts for 41.7% of the total hydrogen release for pure $LiAlH_4$. The excessive decrease in the amount of hydrogen release for the $LiAlH_4$ + 5 mol% $CoFe_2O_4$ samples contributes to the excessive catalytic effect, leading to the complete decomposition of $LiAlH_4$ during the high-energy ball-milling process. In the meanwhile, the dehydrogenation process conducted during the heating and desorption process was the second desorption stage only. Fig. 2 shows hydrogen released from $LiAlH_4$ doped with different amounts of $CoFe_2O_4$, Fe_2O_3 and Co_2O_3 catalysts, which is nearly close to the theoretical hydrogen release content of the pristine $LiAlH_4$. However, when the content of every catalyst is higher than a certain value, the amount of hydrogen released sharply decreases. For the $CoFe_2O_4$ doped $LiAlH_4$ sample, its hydrogen released amount declined quickly when more than 2 mol% $CoFe_2O_4$ nanoparticles were added. However, as for the Fe_2O_3 and Co_2O_3 doped $LiAlH_4$ samples, their hydrogen release content decreases rapidly when the Fe_2O_3 and Co_2O_3 nanoparticles content was more than 5 mol%. $CoFe_2O_4$ has a stronger catalytic effect on the dehydrogenation properties of $LiAlH_4$, compared with Fe_2O_3 and Co_2O_3. The $LiAlH_4$ + 2 mol% $CoFe_2O_4$ sample exhibits optimal dehydrogenation performance, based on the onset dehydrogenation temperature and hydrogen desorption capacity, and would be utilized to analyze the catalytic effect and the mechanism of the $CoFe_2O_4$ nanoparticles in the following tests.

Fig. 3 shows the isothermal dehydrogenation behavior of the as-received $LiAlH_4$ at 120 °C and the $LiAlH_4$ + 2 mol% $CoFe_2O_4$ at 90 °C, 120 °C and 150 °C, respectively. From the curve (a) in Fig. 3, only 0.7 wt% of hydrogen could be detected within 180 min, indicating a perishing desorption kinetics of pristine $LiAlH_4$ at 120 °C. However, the dehydrogenation kinetics of $LiAlH_4$ was significantly enhanced after doping Co ferrite nanopowder. When heated at 90 °C (Fig. 3b), the $CoFe_2O_4$-doped sample could release 5.1 wt% hydrogen within 160 min, suggesting the first dehydrogenation step completion for $LiAlH_4$. Furthermore, the 2 mol% doped sample released 6.8 wt % of hydrogen within 160 min at 120 °C (Fig. 3c), which is 6.1 wt % higher compared with the as-received $LiAlH_4$ for the same heating temperature and time. When further increasing

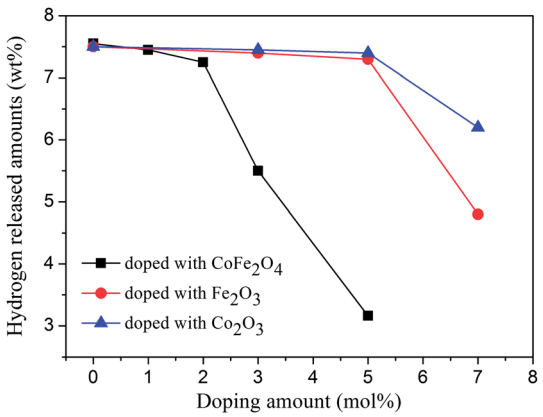

Fig. 2 Hydrogen released from $LiAlH_4$ doped with different catalysts in the 25–250 °C temperature range.

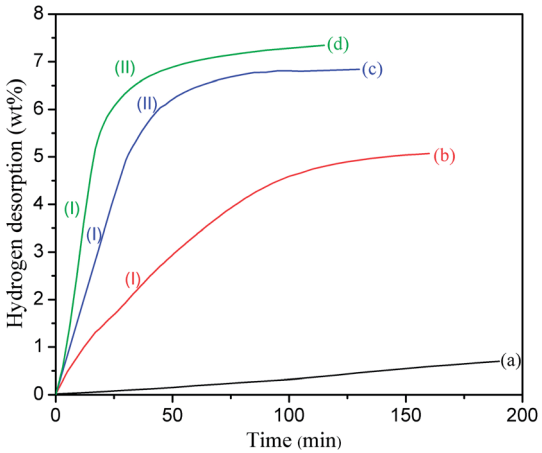

Fig. 3 Isothermal dehydrogenation kinetics of (a) as-received $LiAlH_4$ at 120 °C, and $LiAlH_4$ + 2 mol% $CoFe_2O_4$ at: (b) 90 °C, (c) 120 °C, and (d) 150 °C. (I) represents the first dehydrogenation step, and (II) presses the second dehydrogenation step.

temperature up to 150 °C, only 55 min were required to complete the first two dehydrogenation steps for the $LiAlH_4$ doped with 2 mol% $CoFe_2O_4$, as seen in Fig. 2d. Thus it is reasonable to conclude that $CoFe_2O_4$ exhibits superior catalytic performance and significantly improves the dehydrogenation kinetics of $LiAlH_4$, which makes it quite attractive for the PEM fuel cell applications.

To further reflect the $CoFe_2O_4$ nanoparticles excellent catalytic effect of improving the $LiAlH_4$ isothermal dehydrogenation kinetics and test the practical operating temperature of the PEM fuel cells, Fig. 4 shows isothermal dehydrogenation kinetics of $LiAlH_4$ doped with $CoFe_2O_4$, Fe_2O_3 and Co_2O_3 heated at 90 °C. As seen in Fig. 4, the Co_2O_3 and Fe_2O_3 doped samples release 4.0 wt% and 4.4 wt% H_2 in 180 min at 90 °C, while the $CoFe_2O_4$ doped sample could release 5.1 wt% H_2 within 160 min, indicating that $CoFe_2O_4$ is superior to Fe_2O_3 and Co_2O_3 in improving the dehydrogenation kinetics of $LiAlH_4$. This is in good agreement with the hydrogen released amount results of $LiAlH_4$ doped with these three catalysts (Fig. 2).

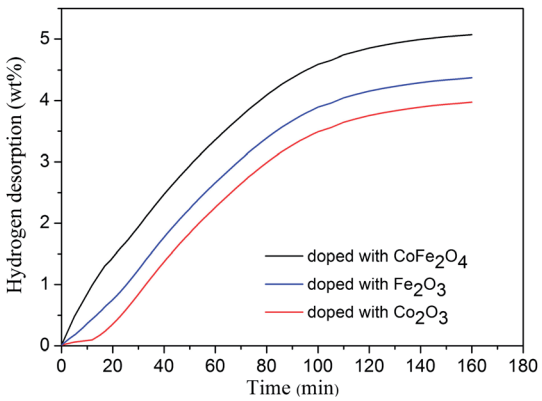

Fig. 4 Isothermal dehydrogenation kinetics of $LiAlH_4$ doped with 2 mol% $CoFe_2O_4$, 5 mol% Fe_2O_3 and 5 mol% Co_2O_3 heated at 90 °C.

In order to further analyze the dehydrogenation steps of the $CoFe_2O_4$ doped samples in terms of the exo/endothermic characteristics and to acquire activation energy (E_a) for each dehydrogenation step according to the Kissinger method, Fig. 5 displays the DSC curves of the as-received $LiAlH_4$ (6 °C min^{-1}) and 2 mol% $CoFe_2O_4$ doped $LiAlH_4$ (6 °C min^{-1}, 9 °C min^{-1} and 12 °C min^{-1}) within the 35–300 °C temperature range, respectively. The as-received $LiAlH_4$ DSC curve contains four characteristic peaks in the first two dehydrogenation steps (two exothermic and two endothermic peaks). These four thermal characteristic peaks correspond to the interaction of $LiAlH_4$ with surface hydroxyl impurities at 154.9 °C, melting of $LiAlH_4$ at 166.4 °C,[54] decomposition of liquid $LiAlH_4$ (R1) at 184.5 °C and decomposition of Li_3AlH_6 at 240 °C (R2).[32] However, the DSC curve of the $CoFe_2O_4$ doped $LiAlH_4$ sample has only two characteristic peaks measured at different heating rates. When heated at a heating rate of 6 °C min^{-1}, the exothermic peak of the doped sample appeared at about 131 °C. Thus the first exothermic peak is attributed to the decomposition of the solid state $LiAlH_4$, since the $CoFe_2O_4$ doped $LiAlH_4$ started to decompose prior to its melting. Then the endothermic peak emerged at 205 °C, corresponding to the dehydrogenation step of Li_3AlH_6. Furthermore, the characteristic temperatures of these two endothermic peaks gradually rise with the increasing heating rate, suggesting that the doped sample has more time to relax at any given temperature and thus the decomposition occurs sooner at a lower temperature when heated at the relatively lower rate. A similar phenomenon is also reported in the DSC results of $LiAH_4$ doped with various catalysts.[13–16,18,32,38,40,43,44] Therefore, the dehydrogenation properties of $LiAlH_4$ were significantly improved by adding $CoFe_2O_4$ nanoparticles, reflecting the remarkable reduction on the characteristic peak temperature of $LiAH_4$.

In order to analyze the catalytic mechanism of $CoFe_2O_4$ nanoparticles on the dehydrogenation properties of $LiAlH_4$, the apparent activation energy (E_a) of the as-received $LiAlH_4$ and the

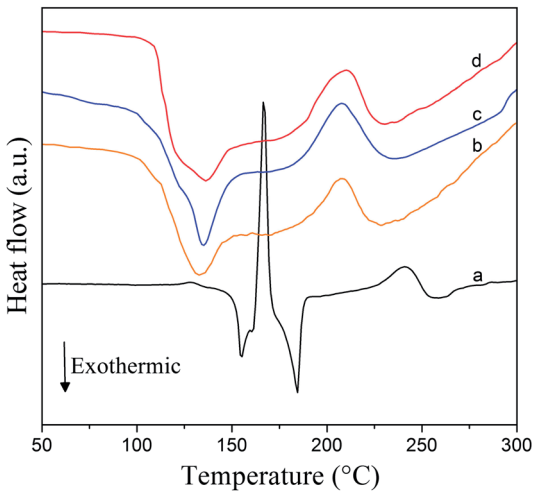

Fig. 5 DSC curves of (a) as-received $LiAlH_4$, $LiAlH_4$ + 2 mol% $CoFe_2O_4$ in the 35–300 °C temperature range and the heating rate of: (b) 6 °C min^{-1}, (c) 9 °C min^{-1}, and (d) 12 °C min^{-1}.

$CoFe_2O_4$-doped $LiAlH_4$ sample for the first two decomposition steps were calculated by using the Kissinger method,[55]

$$\frac{\mathrm{d}\ \ln\left(\frac{\beta}{T_p^{\ 2}}\right)}{\mathrm{d}\left(\frac{1}{T_p}\right)} = -\frac{E_a}{R}, \quad (5)$$

where β, T_p and R express the heating rate, the peak temperature and the gas constant, respectively. Fig. 6 shows the Kissinger plots for the first and second dehydrogenation steps of the as-received $LiAlH_4$ and $LiAlH_4$ + 2 mol% $CoFe_2O_4$. According to the slope of the line in Fig. 6, the E_a values of the as-received $LiAlH_4$ for the first two dehydrogenation steps are calculated to be 94.8 kJ mol^{-1} H_2 and 172.6 kJ mol^{-1} H_2, respectively. Furthermore, the E_a for the two decomposition reactions of the $CoFe_2O_4$ doped sample are 52.4 kJ mol^{-1} H_2 and 86.5 kJ mol^{-1} H_2, which is 42.4 kJ mol^{-1} H_2 and 86.1 kJ mol^{-1} H_2 lower than those of pristine $LiAlH_4$, respectively. Hence, it is reasonable to conclude that the addition of $CoFe_2O_4$ nanopowder has effectively lowered the kinetic barrier for the $LiAlH_4$ decomposition.

In order to compare the change of morphology of the powder samples before/after ball milling and show the distribution of constitution elements of catalyst around the $LiAlH_4$ matrix, Fig. 7 presents the SEM images of the as-received $LiAlH_4$, ball-milled $LiAlH_4$ and the 2 mol% doped $LiAlH_4$ coupled with the elemental maps. As seen in Fig. 7a, the as-received $LiAlH_4$ sample consists of large irregular polyhedron particles, up to 40 μm in size. However, in Fig. 7b, the morphology of the as-milled $LiAlH_4$ became as amounts of regular globular particles with diameter ranging from 3 and 10 μm, reflecting a significant decrease in the particle size of $LiAlH_4$ after ball milling. Fig. 7(c–g) display the SEM images and the corresponding elemental maps of the $LiAlH_4$ + 2 mol% $CoFe_2O_4$ sample after mechanical ball-milling for 30 min. Microscopically, the grains of the $LiAlH_4$ + 2 mol% $CoFe_2O_4$ sample are fine but inhomogeneous, and the original particles were broken into smaller particles

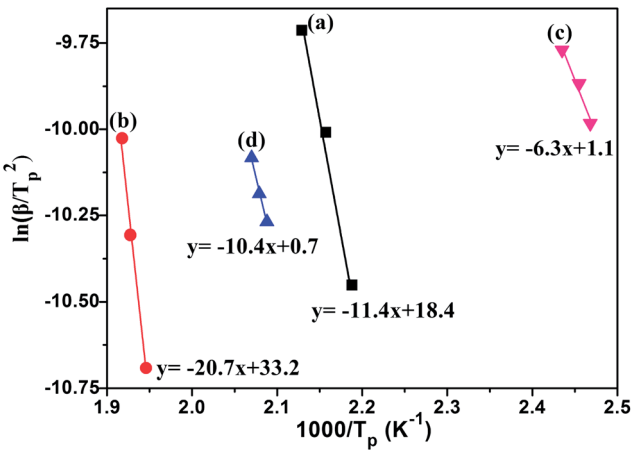

Fig. 6 Kissinger plots for the as-received $LiAlH_4$: (a) the first step and (b) the second step and $LiAlH_4$ doped with 7 mol% $CoFe_2O_4$: (c) the first step and (d) the second step.

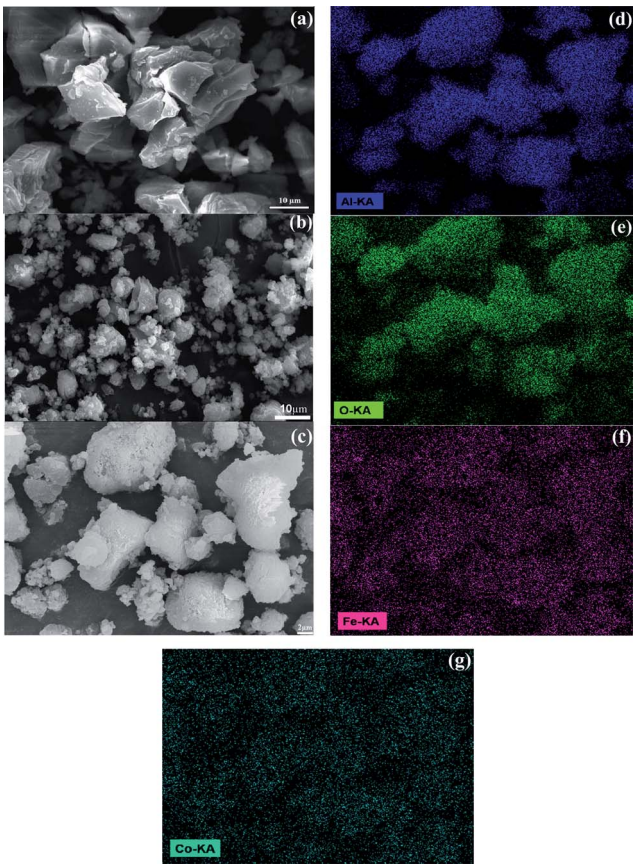

Fig. 7 SEM micrographs of (a) as-received $LiAlH_4$ and (b) $LiAlH_4$ + 2 mol% $CoFe_2O_4$ after ball-milling. (c) SEM micrograph with (d)–(g) corresponding elemental maps of the 2 mol% $CoFe_2O_4$-doped sample.

with the average size of about 6 μm by mechanical ball-milling. The tiny particles have a tendency to assemble and form stepped structures. As seen in Fig. 7(d–g), the elemental maps of constituent elements Al, O, Fe, and Co show uniform distribution of these species in the mixture, indicating that the catalyst of $CoFe_2O_4$ nanopowder could be well mixed with $LiAlH_4$ matrix through high energy ball milling. There is an existing good contact between the $CoFe_2O_4$ catalyst and the $LiAlH_4$ particles, resulting in the significantly enhanced dehydrogenation kinetics of $LiAlH_4$. Nevertheless, through comparison the elemental map O with that of other constituent elements of $CoFe_2O_4$ catalyst, it is worth to note that the elemental map of O has more distribution than that of Fe and Co, which is mainly caused by the oxidation during the specimen preparation process and oxygen element introduced from the conducting resin. Therefore, the high density surface defects and well dispersed catalyst introduce a larger amount of reaction nucleation sites the and hydrogen diffusion channels around the $LiAlH_4$ matrix for the dehydrogenation process, which results in the surface activation and obviously improved dehydrogenation properties of $LiAlH_4$.

IR spectra of the as-received $LiAlH_4$, as-milled $LiAlH_4$ and $LiAlH_4$ doped with 1 mol%, 2 mol%, 3 mol% and 5 mol% $CoFe_2O_4$ samples after ball milling are compared in Fig. 8.

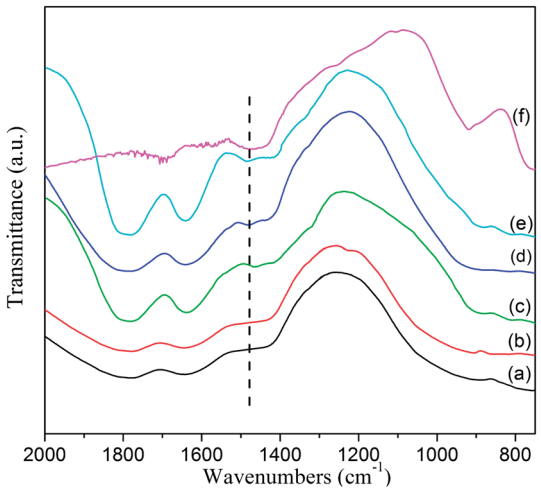

Fig. 8 FTIR spectra of (a) as-received $LiAlH_4$, (b) as-milled $LiAlH_4$ and (c) 1 mol%, (d) 2 mol%, (e) 3 mol% and (f) 5 mol% $CoFe_2O_4$ doped $LiAlH_4$ after ball milling.

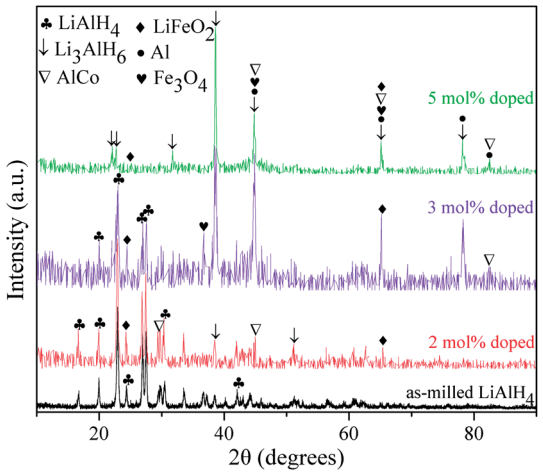

Fig. 9 XRD patterns for the as-milled $LiAlH_4$ and $LiAlH_4$ + 2 mol%, 3 mol% and 5 mol% $CoFe_2O_4$ after ball milling.

According to ref. 14, 24, 28, 40, 44 and 46, the active infrared vibrations of the Al–H bond for $LiAlH_4$ distribute at two regions, corresponding to 1600–1800 cm^{-1} for the Al–H stretching modes and 800–900 cm^{-1} for the Li–Al–H bending modes. While the active infrared vibrations for Li_3AlH_6 exhibit the Al–H stretching modes in the 1500–1400 cm^{-1} region.[14–16,28,44,56] For the $CoFe_2O_4$ doped $LiAlH_4$ samples shown in Fig. 8 (curves c–f), their active infrared vibration of the Al–H stretching modes appear at 1473 cm^{-1}, suggesting the existence of Li_3AlH_6 in the doped sample after ball milling. However, no Al–H bond peak of Li_3AlH_6 is found at the same position in the IR spectra of the as-received and as-milled $LiAlH_4$ (Fig. 8, curves a and b). The absorption intensity of the Li_3AlH_6 peak gradually strengthen with increasing $CoFe_2O_4$ catalyst content, which indicates that the content of Li_3AlH_6 continuously increases resulting from the decomposition proportion of $LiAlH_4$ raise with more $CoFe_2O_4$ catalyst. It is worth to note that the $LiAlH_4$ IR absorption peak cannot be observed when adding 5 mol% $CoFe_2O_4$ nanoparticles into the $LiAlH_4$ matrix, resulting from the 5 mol% $CoFe_2O_4$ doped sample complete decomposition and Li_3AlH_6 formation during the ball milling process. This phenomenon can be confirmed by the nonisothermal dehydrogenation performance of the 5 mol% doped $LiAlH_4$ (Fig. 1). Based on the comprehensive IR spectra analysis, it is concluded that the $CoFe_2O_4$-doped $LiAlH_4$ decomposition reaction occurs, forming the Li_3AlH_6 phase during the ball-milling process. The decomposition reaction of $LiAlH_4$ gradually intensifies with the increasing $CoFe_2O_4$ amount, and the details of the decomposition byproducts would be determined by the following XRD measurements.

The above measurements confirm that some specific stoichiometric reactions between $LiAlH_4$ and $CoFe_2O_4$ occur during the ball-milling process. To clarify the phase transforms between $LiAlH_4$ and $CoFe_2O_4$ during the ball-milling process, Fig. 9 presents the XRD patterns of the as-milled $LiAlH_4$ and $LiAlH_4$ doped with 2 mol%, 3 mol% and 5 mol% $CoFe_2O_4$ after the ball milling process. In the XRD spectra of the as-milled $LiAlH_4$ all diffraction peaks correspond to the $LiAlH_4$ phase, without any additional decomposition products, suggesting that pure $LiAlH_4$ remains rather stable during the ball milling process.[13–16,18,40,43,57,58] This point can also be proven by the non-isothermal dehydrogenation properties of the as-received and as-milled $LiAlH_4$ (Fig. 1), and the FTIR spectra of the as-milled $LiAlH_4$ (Fig. 8). However, compared with the as-milled $LiAlH_4$, the XRD patterns of the $CoFe_2O_4$ doped $LiAlH_4$ samples do not appear as just physical mixtures of $LiAlH_4$ and Co ferrite, which is in a good agreement with the FTIR results (Fig. 8). Adding 2 mol% $CoFe_2O_4$ nanoparticles into the $LiAlH_4$ matrix by mechanical milling causes weak diffraction peaks of microcrystalline aluminum and Li_3AlH_6 to appear in the XRD pattern. Meanwhile, the diffraction peaks of $LiFeO_2$ are observed at 41.3°, 44.7° and 34.8°, and the diffraction peaks at 31.3°and 44.8° correspond to AlCo, while the diffraction peaks of Fe_3O_4 are at 44.8°, and 65.1°. However, the $CoFe_2O_4$ phase could not be detected in the XRD patterns for the doped samples after the ball milling, which demonstrates that the reaction between $LiAlH_4$ and $CoFe_2O_4$ occurred during the ball-milling process. A similar phenomenon also appears in $LiAlH_4$ doped with other documented nanosized catalysts: $MnFe_2O_4$,[14] Fe_2O_3,[15] $NiFe_2O_4$[16] and Nb_2O_5,[44] in which a complete reaction occurs between $LiAlH_4$ and the catalyst precursor, and subsequently the reaction products act as real catalysts for the succeeding decomposition of $LiAlH_4$. With increasing the Co ferrite content up to 3 mol%, the diffraction intensity of the decomposition products of Al, Li_3AlH_6, $LiFeO_2$ and Fe_3O_4 is gradually enhanced. The diffraction intensity of $LiAlH_4$ conspicuously declines, compared with that of 2 mol% doped $LiAlH_4$ sample, signifying that $LiAlH_4$ reacts with $CoFe_2O_4$, resulting in more $LiAlH_4$ decomposition during the ball milling process. Surprisingly, the diffraction peaks of $LiAlH_4$ cannot be observed for the 5 mol % doped sample, and all diffraction peaks correspond to the decomposition products, including $LiFeO_2$, Fe_3O_4, AlCo, Al and Li_3AlH_6, as seen in Fig. 9. This can be explained by the reaction

between $LiAlH_4$ and $CoFe_2O_4$, leading to the complete decomposition of $LiAlH_4$ doped with $CoFe_2O_4$ during the ball milling process, causing the $LiAlH_4$ phase disappearance in the 5 mol% $CoFe_2O_4$-doped sample. In addition, the nano-sized $CoFe_2O_4$ phase cannot be detected in the XRD patterns of all doped samples, mainly because of the complete reaction between $LiAlH_4$ and $CoFe_2O_4$, forming $LiFeO_2$, AlCo, Al and Li_3AlH_6 phases. In the literature, a similar phenomenon has been reported, where NbF_5−,[13] $MnFe_2O_4$−,[14] $NiCl_2$−,[37] TiF_3−,[38] and TiO_2−,[43] as additives for $LiAlH_4$ also could not be detected after high energy ball-milling.

Fig. 10 displays the XRD patterns of the as-milled $LiAlH_4$ and 2 mol%, 3 mol% and 5 mol% $CoFe_2O_4$-doped $LiAlH_4$ after dehydrogenation at 250 °C. The XRD spectra of dehydrogenated as-milled $LiAlH_4$ only consists of Al and LiH phases as the dehydrogenation products, demonstrating that the first two dehydrogenation steps of $LiAlH_4$ have completed upon heating to 250 °C. In contrast, the XRD patterns of the doped samples show the dehydrogenation products containing not only Al and LiH phases, but also $LiFeO_2$, $LiAlO_2$, $Fe_{0.98}O$ and $Al_{0.52}Co_{0.48}$ phases, which is quite different compared with the dehydrogenation products of the as-milled counterpart samples. Moreover, the diffraction peaks of $LiFeO_2$, $LiAlO_2$, $Fe_{0.98}O$ and $Al_{0.52}Co_{0.48}$ phases gradually strengthen with the increasing $CoFe_2O_4$ amount. With respect to the significantly improved dehydrogenation performance of $LiAlH_4$ by doping $CoFe_2O_4$ nanoparticles, *in situ* formed reaction products may act as the catalyst for the first two dehydrogenation steps of $LiAlH_4$. Meanwhile, the reactions occurring during the dehydrogenation processes could facilitate the dehydrogenation dynamics of $LiAlH_4$. These favorable factors together provide a synergetic contribution to the significantly improved dehydrogenation properties of $LiAlH_4$.

The above experimental results demonstrate that the $CoFe_2O_4$ nanopowder plays an important role in improving the dehydrogenation properties of Li alanate. The reasons leading to the significantly improved dehydrogenation properties, acquired in this work for the $CoFe_2O_4$-doped samples, could be summarized as follows: first, previous studies have revealed that the reaction thermodynamics could be affected by reducing the grain size.[59] The smaller particle size and a large number of created surface defects can introduce more reaction nucleation sites and hydrogen diffusion channels for the dehydrogenation process of $LiAlH_4$. Second, $CoFe_2O_4$ reacts with $LiAlH_4$ during the ball-milling process by forming a ternary Li–Fe oxide ($LiFeO_2$), Al–Co compound (AlCo) and Fe oxide (Fe_3O_4) species, suggesting that Co ferrite can transform into other new Co- and Fe-containing phases by increasing the high local temperature (demonstrated in ESI†) during the ball milling process. After dehydrogenation, the $LiFeO_2$, $LiAlO_2$, $Fe_{0.98}O$ and $Al_{0.52}Co_{0.48}$ phases as the dehydrogenation products appear in the XRD patterns, and the diffraction intensity of these products gradually increases with further $CoFe_2O_4$ additive amount. These finely dispersed reaction products serve as the active sites for nucleation and growth of the dehydrogenation products, and the diffusion length of the reaction ions is largely shortened. Third, series of reactions between $LiAlH_4$ and $CoFe_2O_4$ occur by forming a ternary Li–Fe oxide, Fe oxide and Al–Co phases with a reduced valence state during heating. Thus, it is expected that these reactions could alter the reaction thermodynamics by lowering the enthalpy of the dehydrogenation reaction.[44] It is reasonable to conclude that the refinement of the $LiAlH_4$ powder combined with the reactions between $LiAlH_4$ and $CoFe_2O_4$ together contribute to the significantly improved dehydrogenation kinetics of $LiAlH_4$.

In order to comprehensively consider the catalytic effect of nano-sized $CoFe_2O_4$ for $LiAlH_4$, Fig. 11 shows the rehydrogenation results of the 2 mol% doped sample at 140 °C under 6.5 MPa pressure, followed by the subsequent desorption at 250 °C. After complete dehydrogenation during the first two reactions heated up to 250 °C, the sample was rehydrogenated at 140 °C under 6.5 MPa pressure. It is obvious that the rehydrogenation properties of the $CoFe_2O_4$ doped sample reach 0.15 wt% H_2 resorbed for the given conditions. Meanwhile, in order to confirm the rehydrogenation effect, Fig. 11 also provides the XRD pattern of the $LiAlH_4$ + 2 mol% $CoFe_2O_4$ sample after

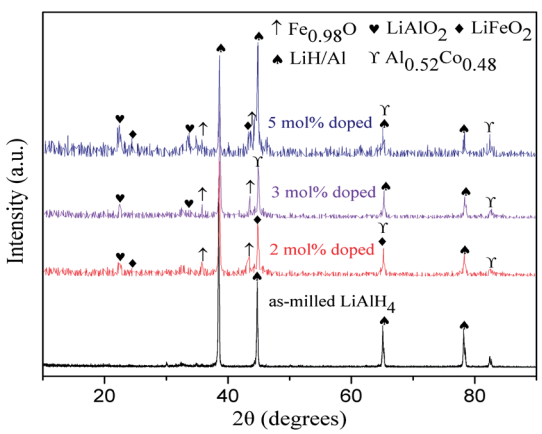

Fig. 10 XRD patterns of the as-milled $LiAlH_4$ and $LiAlH_4$ + 2 mol%, 3 mol% and 5 mol% $CoFe_2O_4$ after dehydrogenation at 250 °C.

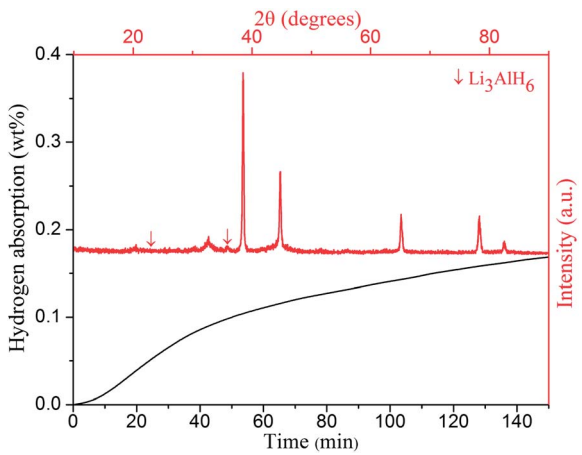

Fig. 11 Rehydrogenation of $LiAlH_4$ + 2 mol% $CoFe_2O_4$ sample and its corresponding XRD pattern after hydrogen resorbtion at 140 °C under 6.5 MPa H_2 for 2.5 h.

resorbing hydrogen for the given conditions in 2.5 h. The XRD spectra of the rehydrogenated sample shows almost identical results with the dehydrogenated sample, except for the appearance of few Li_3AlH_6 peaks, indicating that the second decomposition reaction of $LiAlH_4$ may be partially reversible by the catalytic effects of Co- and Fe-containing products. However, further study of hydrogen storage reversibility of the dehydrogenated $LiAlH_4$ is still underway.

4. Conclusions

In summary, the dehydrogenation properties of $LiAlH_4$ catalyzed by $CoFe_2O_4$ nanoparticles have been substantially improved compared with pure Li alanate powder. The onset desorption temperature of the 2 mol% $CoFe_2O_4$ doped $LiAlH_4$ sample is 65 °C, resulting in 90 °C decrease, compared with the as-received $LiAlH_4$. The rehydrogenation properties of the 2 mol % $CoFe_2O_4$ doped $LiAlH_4$ are inferior for the tested conditions, with 0.15 wt% H_2 resorbtion. The isothermal dehydriding kinetics shows that the $LiAlH_4$ + 2 mol% $CoFe_2O_4$ sample can release 6.8 wt% of hydrogen in 160 min under 0.1 MPa pressure, which is 6.1 wt% higher than that of the pristine $LiAlH_4$ under the same conditions (time, temperature and pressure). Furthermore, through the differential scanning calorimetry and the Kissinger desorption kinetics analyses, the apparent activation energy, E_a, of the 2 mol% $CoFe_2O_4$ doped sample are calculated to be 52.4 kJ mol^{-1} H_2 and 86.5 kJ mol^{-1} H_2 for the first two decomposition reactions, which are 42.4 kJ mol^{-1} H_2 and 86.1 kJ mol^{-1} H_2 lower than those of the pristine $LiAlH_4$, respectively. Based on the FTIR and XRD analyses of the doped samples, a series of reactions occurred between $LiAlH_4$ and $CoFe_2O_4$ during the ball-milling process, forming Al, Li_3AlH_6, $LiFeO_2$, Fe_3O_4, and Fe_3O_4 as decomposition products. These reactions proceeded upon heating, and the $LiFeO_2$, $LiAlO_2$, $Fe_{0.98}O$ and $Al_{0.52}Co_{0.48}$ phases appeared. These *in situ* formed decomposition products, coupled with the reactions, play a synergistic role in remarkably improving dehydrogenation properties of $LiAlH_4$. From the conducted experiments it is reasonable to conclude that $CoFe_2O_4$ nanoparticles play a critical role in the significantly improved $LiAlH_4$ dehydrogenation performance.

Acknowledgements

The authors thank the National High-Tech R&D Program (863 Program) of China (2006AA05Z132) for financial support of this research. Fuqiang Zhai thanks the China Scholarship Council (CSC) for the scholarship.

References

1 L. G. Li, Q. F. Gu, Z. W. Tang, X. W. Chen, Y. B. Tan, Q. Li and X. B. Yu, *J. Mater. Chem. A*, 2013, **1**, 12263–12269.
2 M. Ismail, Y. Zhao, X. B. Yu and S. X. Dou, *RSC Adv.*, 2011, **1**, 408–414.
3 R. Din, X. H. Qu, P. Li, L. Zhang, M. Ahmad, M. Z. Iqbal, M. Y. Rafique and M. H. Farooq, *RSC Adv.*, 2012, **2**, 4891–4903.
4 P. Sridechprasat, L. Phuirot, P. Rangsunvigit, B. Kitiyanan and S. Kulprathipanja, *Energies*, 2012, **5**, 3691–3700.
5 F. Y. Cheng, Z. L. Tao, J. Liang and J. Chen, *Chem. Commun.*, 2012, **48**, 7334–7343.
6 H. Reardon, J. M. Hanlon, R. W. Hughes, A. G. Jopek, T. K. Mandalac and D. H. Gregory, *Energy Environ. Sci.*, 2012, **5**, 5951–5979.
7 A. Borgschulte, A. Jain, A. J. Ramirez-Cuesta, P. Martelli, A. Remhof, O. Friedrichs, R. Gremaud and A. Züttel, *Faraday Discuss.*, 2011, **151**, 213–230.
8 J. C. Fallas, W. M. Chien, D. Chandra, V. K. Kamisetty, E. D. Emmons, A. M. Covington, R. Chellappa, S. A. Gramsch, R. J. Hemley and H. Hagemann, *J. Phys. Chem. C*, 2010, **114**, 11991–11997.
9 Y. B. Tan and X. B. Yu, *RSC Adv.*, 2013, **3**, 23879–23894.
10 D. Lacina, L. Yang, I. Chopra, J. Muckerman, Y. Chabal and J. Graetz, *Phys. Chem. Chem. Phys.*, 2012, **14**, 6569–6576.
11 http://www1.eere.energy.gov/hydrogenandfuelcells/storage/pdfs/targets_onboard_hydro_storage_explanation.pdf.
12 A. Andreasen, T. Veggea and A. S. Pedersena, *J. Solid State Chem.*, 2005, **178**, 3672–3678.
13 M. Ismail, Y. Zhao, X. B. Yu and S. X. Dou, *Int. J. Hydrogen Energy*, 2010, **35**, 2361–2367.
14 F. Q. Zhai, P. Li, A. Z. Sun, S. Wu, Q. Wan, W. N. Zhang, Y. L. Li, L. Q. Cui and X. H. Qu, *J. Phys. Chem. C*, 2012, **116**, 11939–11945.
15 Z. L. Li, P. Li, Q. Wan, F. Q. Zhai, Z. W. Liu, K. F. Zhao, L. Wang, S. Y. Lü, L. Zou, X. H. Qu and A. A. Volinsky, *J. Phys. Chem. C*, 2013, **117**, 18343–18352.
16 P. Li, Z. L. Li, Q. Wan, F. Q. Zhai, X. Q. Li, X. H. Qu and A. A. Volinsky, *J. Phys. Chem. C*, 2013, **117**, 25917–25925.
17 B. Bogdanovic and M. Schwickardi, *J. Alloys Compd.*, 1997, **253**, 1–9.
18 V. P. Balema, V. K. Pecharsky and K. W. Dennis, *J. Alloys Compd.*, 2000, **313**, 69–74.
19 J. Chen, N. Kuriyama, Q. Xu, H. T. Takeshita and T. Sakai, *J. Phys. Chem. B*, 2001, **105**, 11214–11220.
20 V. P. Balema, J. W. Wiench, K. W. Dennis, M. Pruski and V. K. Pecharsky, *J. Alloys Compd.*, 2001, **329**, 108–114.
21 M. Resan, M. D. Hampton, J. K. Lomness and D. K. Slattery, *Int. J. Hydrogen Energy*, 2005, **30**, 1413–1416.
22 X. P. Zheng, P. Li, F. Q. An, G. Q. Wang and X. H. Qu, *Rare Met. Mater. Eng.*, 2008, **37**, 400–403.
23 N. Mehraj-ud-din, R. Sami-ullah, C. S. So, S. W. Hwang, A. R. Kim and K. S. Nahm, *Int. J. Hydrogen Energy*, 2009, **34**, 8937–8943.
24 R. A. Varin and L. Zbroniec, *J. Alloys Compd.*, 2010, **506**, 928–939.
25 H. W. Langmi, G. S. McGrady, X. F. Liu and C. M. Jensen, *J. Phys. Chem. C*, 2010, **114**, 10666–10669.
26 X. F. Liu, H. W. Langmi, S. D. Beattie, F. F. Azenwi, G. S. McGrady and C. M. Jensen, *J. Am. Chem. Soc.*, 2011, **133**, 15593–15597.

27 K. L. Hima, B. Viswanathan and M. S. Srinivasa, *Int. J. Hydrogen Energy*, 2008, **33**, 366–373.
28 R. Din, L. Zhang, P. Li and X. H. Qu, *J. Alloys Compd.*, 2010, **508**, 119–128.
29 L. H. Kumar, C. V. Rao and B. Viswanathan, *J. Mater. Chem. A*, 2013, **1**, 3355–3361.
30 C. P. Hsu, D. H. Jiang, S. L. Lee, J. L. Horng, M. D. Gerb and J. K. Chang, *Chem. Commun.*, 2013, **49**, 8845–8847.
31 W. C. Hsu, C. H. Yang and W. T. Tsai, *Int. J. Hydrogen Energy*, 2014, **39**, 927–933.
32 A. Andreasen, *J. Alloys Compd.*, 2006, **419**, 40–44.
33 J. R. Ares Fernandez, K. F. Aguey-Zinsou, M. Elsaesser, X. Z. Ma, M. Dornheim, T. Klassen and R. Bormann, *Int. J. Hydrogen Energy*, 2007, **32**, 1033–1040.
34 Y. Suttisawat, P. Rangsunvigit, B. Kitiyanana, N. Muangsinb and S. Kulprathipanjac, *Int. J. Hydrogen Energy*, 2007, **32**, 1277–1285.
35 X. P. Zheng, P. Li, I. S. Humail, F. Q. An, G. Q. Wang and X. H. Qu, *Int. J. Hydrogen Energy*, 2007, **32**, 4957–4960.
36 Y. Kojima, Y. Kawai, M. Matsumoto and T. Haga, *J. Alloys Compd.*, 2008, **462**, 275–278.
37 T. Sun, C. K. Huang, H. Wang, L. X. Sun and M. Zhu, *Int. J. Hydrogen Energy*, 2008, **33**, 6216–6221.
38 S. S. Liu, L. X. Sun, Y. Zhang, F. Xu, J. Zhang, H. L. Chu, M. Q. Fan, T. Zhang, X. Y. Song and J. P. Grolier, *Int. J. Hydrogen Energy*, 2009, **34**, 8079–8085.
39 R. A. Varin and L. Zbroniec, *J. Alloys Compd.*, 2011, **509S**, S736–S739.
40 Z. B. Li, S. S. Liu, X. L. Si, J. Zhang, C. L. Jiao, S. Wang, S. Liu, Y. J. Zou, L. X. Sun and F. Xu, *Int. J. Hydrogen Energy*, 2012, **37**, 3261–3267.
41 J. Fu, L. Röntzsch, T. Schmidt, M. Tegel, T. Weißgärber and B. Kieback, *Int. J. Hydrogen Energy*, 2012, **37**, 13387–13392.
42 X. P. Zheng, J. J. Zheng, Q. H. Ma, S. L. Liu, X. Feng, X. B. Lin and G. Xiao, *J. Alloys Compd.*, 2013, **551**, 508–511.
43 M. Ismail, Y. Zhao, X. B. Yu, I. P. Nevirkovets and S. X. Dou, *Int. J. Hydrogen Energy*, 2011, **36**, 8327–8334.
44 R. Din, X. H. Qu, P. Li, L. Zhang and M. Ahmad, *J. Phys. Chem. C*, 2011, **115**, 13088–13099.
45 X. P. Zheng and S. L. Liu, *J. Alloys Compd.*, 2009, **481**, 761–763.
46 M. Ismail, Y. Zhao, X. B. Yu, A. Ranjbar and S. X. Dou, *Int. J. Hydrogen Energy*, 2011, **36**, 3593–3599.
47 S. S. Liu, Z. B. Li, C. L. Jiao, X. L. Si, L. N. Yang, J. Zhang, H. Y. Zhou, F. L. Huang, Z. Gabelica, C. Schick, L. X. Sun and F. Xu, *Int. J. Hydrogen Energy*, 2013, **38**, 2770–2777.
48 L. Li, F. Y. Qiu, Y. J. Wang, Y. N. Xu, C. H. An, G. Liu, L. F. Jiao and H. T. Yuan, *Int. J. Hydrogen Energy*, 2013, **38**, 3695–3701.
49 L. Li, Y. N. Xu, Y. Wang, Y. J. Wang, F. Y. Qiu, C. H. An, L. F. Jiao and H. T. Yuan, *Dalton Trans.*, 2014, **43**, 1806–1813.
50 X. F. Liu, S. D. Beattie, H. W. Langmi, G. S. McGrady and C. M. Jensen, *Int. J. Hydrogen Energy*, 2012, **37**, 10215–10221.
51 U. Eberle, M. Felderhoff and F. Schüth, *Angew. Chem., Int. Ed.*, 2009, **48**, 6608–6630.
52 S. Orimo, Y. Nakamori, J. R. Eliseo, A. Züttel and C. M. Jensen, *Chem. Rev.*, 2007, **107**, 4111–4132.
53 M. George, S. S. Nair, K. A. Malini, P. A. Joy and M. R. Anantharaman, *J. Phys. D: Appl. Phys.*, 2007, **40**, 1593–1602.
54 M. McCarty, J. N. Maycock and V. R. P. Verneker, *J. Phys. Chem.*, 1968, **72**, 4009–4014.
55 H. E. Kissinger, *Anal. Chem.*, 1957, **29**, 1702–1706.
56 S. S. Liu, Y. Zhang, L. X. Sun, J. Zhang, J. N. Zhao, F. Xu and F. L. Huang, *Int. J. Hydrogen Energy*, 2010, **35**, 4554–4561.
57 R. A. Varin, L. Zbroniec, T. Czujko and Z. S. Wronski, *Int. J. Hydrogen Energy*, 2011, **36**, 1167–1176.
58 P. B. Amama, J. T. Grant, P. J. Shamberger, A. A. Voevodin and T. S. Fisher, *J. Phys. Chem. C*, 2012, **116**, 21886–21894.
59 J. Lu, Y. J. Choi, Z. Z. Fang, H. Y. Sohn and E. Ronnebro, *J. Am. Chem. Soc.*, 2009, **131**, 15843–15852.